Joint Special Interest Group meeting between euspen and ASPE
Advancing Precision in Additive Manufacturing
TU Berlin, Germany, October 2025
www.euspen.eu

Low-Energy Laser Powder Bed Fusion of Tin-Bronze Alloys for the Production of Grinding Tools

Eckart Uhlmann[1, 2], Duc Anh Khuc[1]

[1]*Institute for Machine Tools and Factory Management (IWF), Technische Universität Berlin, Germany*
[2]*Fraunhofer Institute for Production Systems and Design Technology IPK, Germany*

khuc@tu-berlin.de

Abstract

Tin-bronze alloys with high tin content are commonly used for metal-bonded grinding tools, but their processing by Laser Powder Bed Fusion (PBF-LB/M) remains underexplored. This study focuses on developing PBF-LB/M parameters for bronze alloys CuSn20 and CuSn40 to achieve high workpiece density at minimal energy input, enabling future integration of heat-sensitive abrasives like coated Cubic Boron Nitride (CBN) or diamond. Cubic workpieces were manufactured under varied laser power and exposure time while other parameters remained constant. Both of the alloys investigated reached high density, and a higher tin content led to reduced energy demand, due to improved laser absorptivity and a lower melting temperature of tin compared to copper. However, cracking was observed in all cubic workpieces, likely caused by thermally induced residual stresses. Despite this, the results confirm the feasibility of processing high-tin bronzes with PBF-LB/M for potential application in metal-bonded high-performance grinding tools. Further research will address crack reduction and abrasive integration. These findings contribute to expanding PBF-LB/M-compatible materials for functional tool production.

Keywords: laser powder bed fusion, 3D printing, grinding, alloy, diamond, bronze

1. Introduction

Metal-bonded abrasive grinding tools are used in high-precision manufacturing, particularly for machining difficult-to-cut materials such as ceramics, carbides and superalloys [1, 2]. These tools require a bond matrix that provides strong embedding of abrasive, thermal stability and high wear resistance. Bronze-based alloys, particularly high-tin bronzes, such as CuSn20 and CuSn40, provide an excellent matrix for embedding abrasives such as diamond [1, 3]. These material combinations are typically available as conventional products on the market, including sintered tin-bronze bonded diamond grinding tools [3]. However, the performance of these densely sintered grinding tools is limited due to their low porosity [1, 4, 5].

With the development of additive manufacturing, particularly laser powder bed fusion (PBF-LB/M), there has been increasing interest in manufacturing grinding tools with integrated cooling channels and customised porous structures [6, 7, 8]. Nevertheless, processing copper-based materials using PBF-LB/M remains challenging due to the high laser reflection and thermal conductivity [9, 10]. Although the use of copper and low-tin bronze alloys in PBF-LB/M has been studied, high-tin bronzes has not been subject to recent investigations. Previous research has primarily focused on enhancing laser absorption and optimizing process parameters for copper alloys [8, 11]. However, the specific relationship between higher tin content material, energy input applied during processing and resulting density ρ of manufactured workpieces has hardly been investigated. Despite the established use as bonding materials in conventional metal-bonded grinding tools, high-tin bronzes have so far been scarcely investigated in additive manufacturing, particularly regarding thermal stability and embedding of abrasive.

This study addresses this gap by evaluating the PBF-LB/M-process of high-tin bronze alloys CuSn20 and CuSn40 with focus on achieving high-density workpieces with minimal energy input. The study examines how key process parameters, particularly laser power P_L and exposure time t_{exp}, influence workpiece quality. First, the manufacturing processes, materials and procedures used are presented. The results are then shown, including an analysis of workpiece density ρ and an investigation of defects such as cracks and pores. The effects of laser power P_L and exposure time t_{exp} on workpiece properties and thus on future tool design and the integration of abrasive particles, are then discussed. Finally, the most important results of the present study are summarized and the next steps towards manufacturing of functional grinding tools with PBF-LB/M are outlined.

2. Materials and Methods

2.1. Materials

The high-tin bronze alloys CuSn20 and CuSn40 used in this study are typical bonding materials in metal-bonded high-performance grinding tools due to their good wear resistance and ability to retain abrasive particles. The powders were supplied upon special request by a commercial powder manufacturer and are specifically designed for PBF-LB/M. Both powders have a mostly ball-shaped morphology which enables good integration into the PBF-LB/M-manufacturing system and can be homogeneously distributed on the powder bed. The grain diameter d_g is within the range of 0 µm < d_g ≤ 63 µm. To assess the morphology and surface characteristics of the powder particles, scanning electron microscopy (SEM) was performed. SEM images reveal predominantly ball-shaped, gas-atomized

particles, accompanied by a considerable number of smaller particles which are partly ball-shaped and partly irregular in shape, as exemplified in figure 1. The chemical composition of CuSn20 and CuSn40 corresponds to typical industrial specifications, with mass fraction of tin $w_{Sn,CuSn20}$ = 20 % and $w_{Sn,CuSn40}$ = 40 %, respectively. Since the use of CuSn20 and CuSn40 alloys in additive manufacturing is uncommon, the reference densities $\rho_{ref,CuSn}$ of fully dense workpieces made from these materials are not existing. Therefore, a reference density $\rho_{ref,CuSn}$ for bronze alloys in the range of 8.80 g/cm³ ≤ $\rho_{ref,CuSn}$ ≤ 8.90 g/cm³ is assumed, based on information of powder suppliers [12, 13]. In the following analyses, absolute densities ρ_{abs} are used to enable a precise assessment of the density of the additively manufactured workpieces.

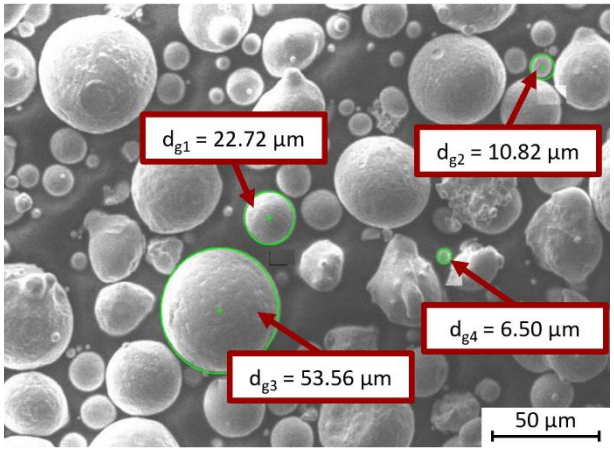

Figure 1. SEM images of CuSn20 powder particles.

2.2. Manufacturing process

The RenAM-500Q PBF-LB/M-system from RENISHAW PLC, Wotton under Edge, England, is used to process the high-tin alloy powders. This system is equipped with four independently controllable ytterbium infrared fibre lasers, each operating at a wavelength of λ = 1,070 nm and a maximum laser power of $P_{L,max}$ = 500 W. It also features an automated powder feed and recycling system. The laser focus diameter is d_L = 80 µm. High purity argon gas is used to inertise the chamber to a minimum oxygen concentration of $c_{oxygen,min} = 100 \cdot 10^{-6}$. In the PBF-LB/M-process, workpieces are built additively layer by layer. After each selective laser exposure based on the digital geometry data of the workpiece, a new layer of powder is deposited by the recoater to enable the subsequent melting step. The two alloy powders CuSn20 and CuSn40 were introduced individually into the PBF-LB/M-system for the tests. The system was cleaned between the investigations with the two different alloys to prevent cross-contamination.

Cubic workpieces with a base area of A_G = 10 mm · 10 mm and a height of h = 10 mm were manufactured using the mentioned PBF-LB/M-system. Layer thickness s = 60 µm, hatch distance d_h = 90 µm and the scan strategy using a meander pattern with unidirectional, parallel scan lines were kept constant throughout all tests for both CuSn20 and CuSn40 powders. The build platform preheat temperature was set to $\theta_{pre,CuSn20}$ = 150 °C for CuSn20 and $\theta_{pre,CuSn40}$ = 100 °C for CuSn40 to reduce thermal gradients and minimize the risk of cracking.

To systematically develop the process parameters and examine the influence of energy input on workpiece quality, laser power P_L and exposure time t_{exp} were varied over a broad range. The tested settings of these two parameters are summarized in table 1. For each parameter combination, two identical cubic workpieces were produced to ensure the reproducibility of the process.

Table 1. Summary of parameter settings.

Material	Laser power P_L/W	Exposure time t_{exp}/µs
CuSn20	150	50
	250	100
	350	150
CuSn40	100	50
	200	60
	220	70
	240	80
	260	100
	300	150

2.3. Measurement method

The manufactured cubic workpieces were first characterized by density measurements using the archimedes principle based on liquid displacement. Isopropanol was used to remove powder residues from the workpieces immediately after production and to wet them during the density measurement. Following density determination, the workpieces were cut to expose a central cross-section for microscopic analysis. The internal structure and defect morphology were examined using the 3D-digital microscope VHX-5000 from KEYENCE DEUTSCHLAND GMBH, Neu Isenburg, Germany. These microscopic investigations focused on the identification and distribution of porosity and cracks within the workpieces. The results were used to correlate process parameters with workpiece density ρ, and defect formation was qualitatively examined through visual analysis to support future optimization of the PBF-LB/M-process for high-tin bronze alloys.

3. Results

Many of the tested parameter combinations proved unsuitable for the PBF-LB/M-process and led to an early termination of the build jobs after a marginal amount of layers. This was mainly due to severe workpiece deformation, intense smoke emission and excessive spatter formation. Such phenomena have been observed, for example, for CuSn40 with excessive laser power P_L = 300 W and long exposure time t_{exp} = 150 µs. Workpieces could not be built successfully under these unstable conditions and were therefore excluded from further analysis. Subsequently, parameter combinations that enabled the successful manufacturing of cubic workpieces were included in the evaluation. Representative microscopic images of the workpiece surface and the surface of the cut workpiece are shown in the following section. The measured absolute density ρ_{abs} of the manufactured workpieces are shown graphically in relation to the varied process parameters.

Numerous macroscopic cracks and sintered unmelted powder particles were observed on the surfaces of the CuSn20 workpieces. Analysis of the surface of the cut workpiece revealed porosity of varying size and morphology randomly distributed throughout the material. Representative examples of these structural defects, both on the surface and the central cross-section of the workpieces, are shown in figure 2. While the number of defects observed varied slightly between workpieces, generally a high amount of defects was observed consistently in all CuSn20 workpieces.

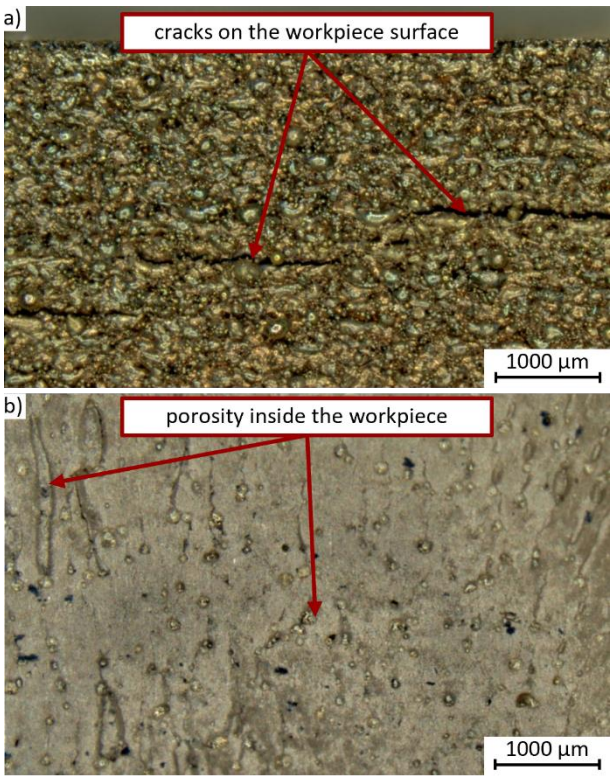

Figure 2. Microscopic images of the CuSn20 workpiece manufactured at P_L = 350 W and t_{exp} = 50 µs; a) Workpiece surface; b) Cross-section of the workpiece.

The measured absolute densities ρ_{abs} of the CuSn20 cubic workpieces range between 8.52 g/cm³ ≤ $\rho_{abs,\ CuSn20}$ ≤ 8.91 g/cm³. Figure 3 illustrates the absolute densities ρ_{abs} in relation to laser power P_L and exposure time t_{exp}. For the exposure time t_{exp} = 100 µs, the density ρ_{abs} remains nearly constant regardless of increasing laser power P_L. In contrast, at exposure time t_{exp} = 50 µs, a degressive correlation between laser power P_L and absolute density ρ_{abs} is observed. Conversely, for exposure time t_{exp} = 150 µs, the density ρ_{abs} increases with higher laser power P_L.

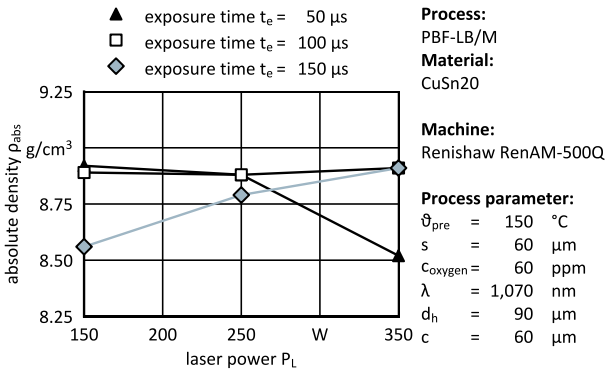

Figure 3. Absolute density ρ_{abs} of CuSn20 workpieces depending on laser power P_L and exposure time t_{exp}.

Compared to the CuSn20 workpieces, the CuSn40 workpieces had significantly fewer macroscopic surface cracks and a decreases amount of unmelted sintered powder particles. Cross-sectional observations of the workpieces show almost no visible porosity or cracking. Figure 4 displays representative images of the surface and the central cross-section of a CuSn40 workpiece. Notably, the inner structure of the illustrated workpiece shows pronounced density without major defects. However, this is only partially observed regarding the entirety of manufactured workpieces. Although the extent and distribution of process-induced defects vary slightly between CuSn40 workpieces, the number of defects is substantially lower compared to CuSn20 workpieces.

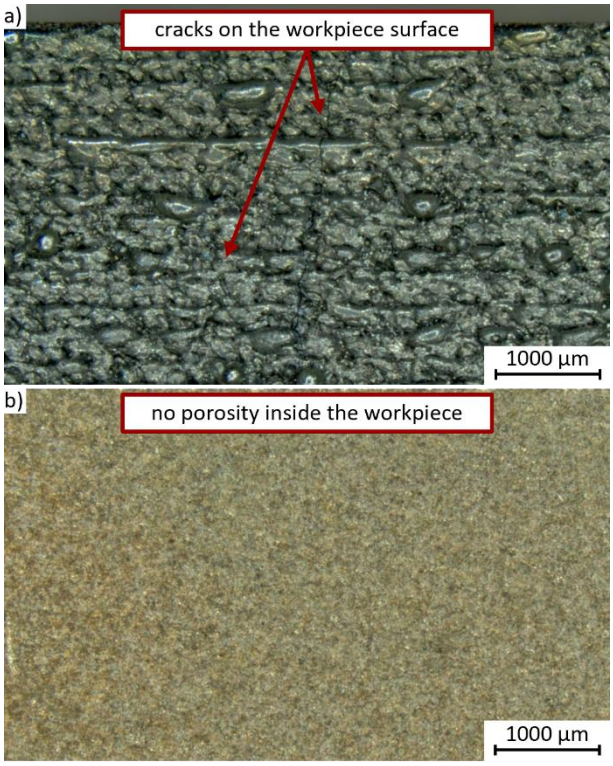

Figure 4. Microscopic images of the CuSn40 workpiece manufactured at P_L = 240 W and t_{exp} = 60 µs; a) Workpiece surface; b) Cross-section of the workpiece.

The measured absolute densities ρ_{abs} of the CuSn40 workpieces show a relatively narrow range of 8.87 g/cm³ ≤ $\rho_{abs,CuSn40}$ ≤ 8.93 g/cm³. Figure 5 presents how the absolute density ρ_{abs} of CuSn40 workpieces varies with changes in laser power P_L and exposure time t_{exp}. Overall, the density ρ_{abs} values show only minor variation with increasing laser power P_L. At the shortest exposure time t_{exp} = 60 µs, the highest absolute density $\rho_{abs,CuSn40}$ = 8.93 g/cm³ was achieved.

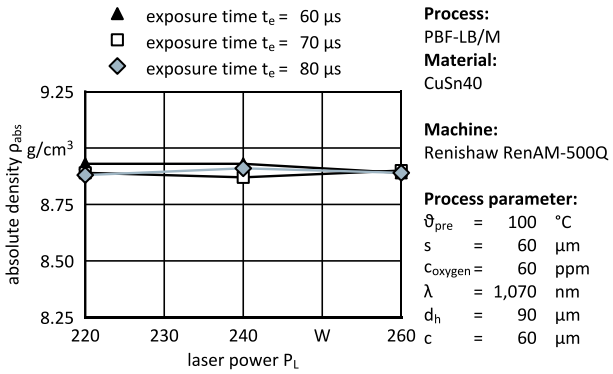

Figure 5. Absolute density ρ_{abs} of CuSn40 workpieces depending on laser power P_L and exposure time t_{exp}.

4. Discussion

For CuSn20 workpieces, the measured absolute densities ρ_{abs} are distributed on a wide range and are in some cases significantly below the assumed reference density $\rho_{ref,\ CuSn}$ for

bronze alloys 8.80 g/cm³ ≤ ρ_{CuSn} ≤ 8.90 g/cm³. Even in cubic workpieces with the highest absolute densities *of* $\rho_{abs,CuSn20}$ = 8.90 g/cm³, structural defects such as porosity and cracking are still visible. The prevalence of such defects suggests excessive energy input or suboptimal exposure time t_{exp} during the PBF-LB/M-process. As indicated in figure 3, reducing the laser power P_L at exposure times of t_{exp} = 50 µs and t_{exp} = 100 µs results in either comparable or improved absolute densities ρ_{abs} with a visible reduction in porosity. These findings suggest that further reducing the energy input may positively influence workpiece quality by minimizing defect formation. However, this conclusion should be treated with caution, as density measurements based on the archimedes method may be inaccurate in workpieces with significant internal defects such as cracks and pores. These defects can lead to unintended displacement effects during immersion and thereby distort the measured density ρ.

For CuSn40, the absolute densities ρ_{abs} is within a narrow range and in some cases exceed the assumed reference density $\rho_{ref,CuSn}$ for bronze alloys. Since the density values show only minor variation across different energy input levels, a reduction in laser power P_L appears feasible in order to improve energy efficiency while still achieving high density and minimizing the risk of defect formation. Moreover, figure 5 indicates that shorter exposure times t_{epx} can lead to slightly higher absolute density ρ_{abs}, further supporting the optimization of process parameters towards lower energy input. Given the relatively low occurrence of process-induced defects in CuSn40 workpieces, the density measurements are considered more reliable compared to those of CuSn20. The reduced presence of internal flaws minimizes potential inaccuracies in the archimedes method and allows robust conclusions regarding the influence of process parameters on correlation between process parameters and absolute density $\rho_{abs,CuSn40}$.

5. Conclusion and Outlook

This study demonstrated the feasibility of processing the high-tin bronze alloys CuSn20 and CuSn40 using PBF-LB/M. The focus was on determining a correlation between process parameters, specifically laser power P_L and exposure time t_{exp}, and workpiece density ρ and defect formation. The results suggest that both alloys achieve high absolute densities ρ_{abs}, with CuSn40 workpieces in particular being produced at nearly full density and exhibiting almost no visible porosity under optimized process parameters. CuSn20 workpieces show a range of absolute densities 8.52 g/cm³ ≤ $\rho_{abs,CuSn20}$ ≤ 8.91 g/cm³ and tend to form an increased amount of defects such as pores and cracks. In contrast, CuSn40 workpieces showed significantly fewer defects and a decreased range of absolute densities 8.87 g/cm³ ≤ $\rho_{abs,CuSn40}$ ≤ 8.93 g/cm³, occasionally exceeding the typical reference density $\rho_{ref,Cusn}$ for bronze alloys. Reducing the energy input by lowering the laser power P_L or shortening the exposure time t_{epx} proved beneficial for both alloys, with CuSn40 demonstrating increasing process robustness and stability. CuSn40 therefore emerges as a particularly promising material for the additive manufacturing of metal-bonded grinding tools. Its low defect formation and suitability for low-energy processing suggests that sensitive abrasive particles can be integrated without causing significant thermal damage.

Future work will focus on further process optimisation to minimise residual stresses and crack formation, especially in CuSn20. Additionally, the integration of coated abrasive grains will be investigated to assess manufacturing of metal-bonded high-performance grinding tools via PBF-LB/M.

References

[1] Klocke F 2017 *Fertigungsverfahren 2: Zerspanung mit geometrisch unbestimmter schneide* (Wiesbaden, Germany: Springer Vieweg)

[2] Denkena B and Tönshoff H K 2011 *Spanen Grundlagen* (Heidelberg, Germany: Springer)

[3] Paucksch E, Holsten S, Linß M and Tikal F 2008 *Zerspantechnik: Prozesse, Werkzeuge, Technologien* (Heidelberg, Germany: Springer)

[4] Tian C, Li X, Zhang S, Guo G, Wang L and Rong Y 2018 Study on design and performance of metal-bonded diamond grinding wheels fabricated by selective laser melting (SLM) *Materials and Design* **156** (Amsterdam, Holland: Elsevier) p 52-61

[5] Ding W F, Xu J H, Chen Z Z, Yang C Y, Song C J and Fu Y C 2013 Fabrication and performance of porous metal-bonded CBN grinding wheels using alumina bubble particles as pore-forming agents *The International Journal of Advanced Manufacturing Technology* **67** (Heidelberg, Germany: Springer) p 1309-1315

[6] Behrens L 2019 Additiv gefertigte CBN- und Diamantschleifbeläge *Diamond Business* (Frankfurt, Germany: VDW GmbH)

[7] Du Z J, Zhang F L, Xu Q S, Huang Y J, Li M C, Huang H P, Wang C Y, Zhou Y M and Tang H Q 2019 Selective laser sintering and grinding performance of resin bond diamond grinding wheels with arrayed internal cooling holes *Ceramics International* **45** (Amsterdam, Holland: Elsevier) p 20873-20881

[8] Ai Q, Khosravi J, Azarhoushang B, Daneshi A, and Becker B 2022 Digital light processing-based additive manufacturing of resin bonded SiC grinding wheels and their grinding performance *The International Journal of Advanced Manufacturing Technology* **118** (Heidelberg, Germany: Springer) p 1641-1657

[9] Tanaka T and Isono Y 2001 New development of a grinding wheel with resin cured by ultraviolet light *Journal of materials processing Technology* **113** (Amsterdam, Holland: Elsevier) p 385-391

[10] Huang Q Y, Guo L and Marinescu I 2015 The Abrasion Mechanism of a Diamond Grinding Wheel with Resin Cured by Ultraviolet Light *Applied Mechanics and Materials* **809** (Bäch, Switzerland: Trans Tech Publications Ltd.) p 21-26

[11] Tanaka T and Okushima K 2003 Development of Grinding Wheels by Stereolithography and Investigation of their Characteristics *Key Engineering Materials* (Bäch, Switzerland: Trans Tech Publications Ltd.) p 277-282

[12] Shanghai Truer Technology Co. Ltd 2024 Specifications of CuSn20 Powder Models *CuSn20 Powder* https://am-material.com/nickel-based-powders/cusn20-powder-20241106/ accessed 20 June 2025

[13] Metal3DP Technology Co. LTD 2024 Properties and Characteristics of CuSn40 Powder *CuSn40 Powder: Maximize Performance in Harsh Environments* https://met3dp.com/cusn40-powder-maximize-performance-harsh-environments/ accessed 20 June 2025